nature photonics

Supplementary information https://doi.org/10.1038/s41566-026-01916-0

An on-chip programmable valley optoelectronic nanocircuit

In the format provided by the authors and unedited

This PDF file includes:

Methods

Numerical simulation:

1) Far-field scattering/Near-field absorption: A 2D model of a thin Si_3N_4 slab waveguide on an SiO_2 substrate was constructed in COMSOL Multiphysics to calculate scattering and absorption. The waveguide mode, numerically calculated at one end of the waveguide, served as the input wave source. A 3-nm-thick WSe_2 layer (n = 4.49, k = 0.75 at wavelength of 620 nm) was included in the model. Perfectly matched layers were applied at the top and bottom boundaries of the simulation domain. See Fig. S1 and Supplementary text for more details and discussions.

2) Metasurface: A home-built rigorous coupled-wave analysis (RCWA) solver was used for parametric sweeps. The modelling details are illustrated in Fig. S2 and explained in *Supplementary Note 2*.

3) Meta-waveguide: 3D models of a Si_3N_4 waveguide and metasurface were constructed in COMSOL Multiphysics (Figs. S3, S4). For the full-wave simulations in Fig. 2b and 2c, 49 electric dipoles were positioned at a fixed distance (*d, d =10 nm*) above the meta-waveguide. A pair of periodic boundary conditions was applied along the x-axis, simulating an infinitely large slab waveguide. Forty-nine meta-atoms were placed along the waveguide with a fixed rotation angle of 124.6°. In the distance dependent simulation in Fig. 2d, either a plane wave or 2D dipole array in a circular region placed as the input source. In Fig. S7, 9 dipoles were set and located either at the centre of the metasurface or shifted (d =10 nm). The refractive indices of amorphous silicon and Si_3N_4 were set as wavelength-dependent, based on experimentally characterized results (not shown). Two domain probes were placed inside the waveguide, 30λ away from the metasurface regions, to detect the coupled field.

Meta-waveguide and photodetector chip fabrication:

The VMP chip fabrication involves fabrication of waveguide, grating coupler, metasurface and the photodetectors. Details on meta-waveguide and photodetector are discussed in Fig. S5 and related discussion in Supplementary text.

Optical characterisation of chirality-selective meta-waveguide:

Wavelength-dependent and polarisation-dependent light routing was characterised by illuminating the metasurface with a wavelength tunable laser (Fianium superK picosecond laser). The laser beam was focused onto the metasurface using a 20x objective lens (Nikon, 0.45 NA), and the reflected light was collected through the same objective lens in a reflective configuration. The scattered light was captured by CCD cameras (Thorlabs, models CS165CU and CS126MU). Polarisation control was achieved using a linear polariser and a quarter-wave plate mounted on a stepper motor rotation mount (Thorlabs, K10CR2). Note that the field of view of our imaging system (objective lens: 20×, NA = 0.45, ~200 μm) fully covers the metawaveguide device, which spans 120 μm. Data processes enabled by python scripts that extract pixel values from the region of interest of images. The related results and optical setup are illustrated in Fig. S6 and Fig. S8, respectively.

Photoluminescence and second-harmonic generation characterisation:

PL measurements and SHG spectra were collected using an Andor spectrograph (Kymera 328i) coupled with an EMCCD camera (iXon Ultra 888). Appropriate colour filter sets were used to block the laser wavelengths. A Fianium laser was employed for PL measurements (Fig. S9b,9c,9d), while a Ti:sapphire femtosecond laser (Chameleon Compact OPO-Vis) was used for SHG measurements (Figs. S9e,9f,9g, S10). The related optical setup is illustrated in Fig. S8.

Optoelectronic characterisation of chirality-selective meta-waveguides:

1). TMDC-based photodetector characterisation: a source meter (Keithley 2450) was employed to bias the WSe_2 photodetector as well as monitor the photocurrent variation. An electrical shutter (Thorlabs, SH05R) was utilized to control the on/off state of the input laser. A 620-nm picosecond pulse laser was focused on either photodetector or metasurface.

2). VMP device characterisation: a low noise current amplifier (SR570) and Oscilloscope (TDS 2014C) were employed to bias the VMP device as well as monitor the photocurrent. A chopper (Thorlabs, MC2000, MC1F10 blade) was used to control the on/off state of the laser at 20 Hz. The device operates over a frequency range of 20 Hz to 10 kHz. A 1240 nm pulsed femtosecond laser was focused on the sandwiched monolayer WS_2.

Supplementary Text

Far-field and near-field collection of waveguide-routed photons

Valley photons in waveguides are conventionally detected in the far field using a microscope that collects scattered light. Consider a slab waveguide (Si_3N_4, 350 nm thick) on an SiO_2 substrate. In the simplest end-scattering configuration, as shown in Figure S1(a), light reflects and scatters at the end surface of the waveguide. Large scattering angles result in limited light collection efficiency in the far field. In contrast, placing a thin TMDC flake (e.g., 3-nm-thick WSe_2, equivalent to 5 layers) directly on the waveguide, as depicted in Figure S1(b), enables the flake to absorb the evanescent field extending from the waveguide surface during light propagation. Due to the high absorption of 2D material, this configuration allows for light detection within a small footprint and significantly enhances collection efficiency.

Numerical simulations were conducted to evaluate far-field collection efficiency and near-field absorptance for varying numerical apertures (NAs) and flake lengths in two scenarios. Far-field collection efficiency is defined as the fraction of power flow above and within the waveguide. Near-field absorptance is defined as the waveguide propagation loss in the flake-covered region. Figure S1(c) summarizes the two scenarios. Far-field collection efficiency strongly depends on the NA of the objective lens. Assuming no optics-induced losses, a moderate NA of 0.6 collects only ~5% of the guided light, while an NA of 0.9 achieves a maximum of ~20%. In contrast, near-field absorption increases with flake length, and a flake length of 50 μm can achieve near-unity collection efficiency.

Nanofabrication processes for the VMP device

Figure S5 illustrates the fabrication process for the VMP device. We begin with quartz substrates (Fig. S5a 1), which are pre-patterned and deposited with global markers for electron-beam lithography (EBL) alignment. First, a 350 nm layer of Si_3N_4 is grown on the quartz substrate using plasma-enhanced chemical vapor deposition (PECVD) (Fig. S5a 2). Next, a 500 nm layer of ZEP520 is spin-coated onto the substrate, followed by soft baking at 180°C for 3 minutes on a hotplate. An ultrathin layer of conductive polymer (Elektra92, ~50 nm) is then spin-coated and baked at 90°C for 1 minute. EBL is used to write the waveguide and grating coupler patterns, which are subsequently developed in n-amyl acetate for 60 seconds and rinsed in isopropyl alcohol (IPA). The substrate is then transferred to a vacuum chamber for inductively coupled plasma reactive ion etching (ICP-RIE), removing approximately 150 nm of Si_3N_4 to form a rib waveguide with shallowly etched grating couplers (Fig. S5a 3). Residual ZEP is removed using O_2 plasma.

Next, a 250 nm layer of amorphous silicon is deposited on the sample for the subsequent metasurface fabrication (Fig. S5b 1). The EBL steps are repeated to define the metasurface patterns. A 30 nm layer of chromium (Cr) is then deposited as a hard mask using electron-beam evaporation. After ICP-RIE etching to transfer the metasurface nanostructures into the amorphous silicon, the Cr mask is removed through wet etching (Fig. S5b 2). Prior to fabricating the photodetectors, gold structures are deposited to serve as the bottom electrodes (Fig. S5b 3).

The last step is to transfer WS_2 to the metasurface and then fabricate two photodetectors (Fig. S5c) to achieve the VMP device. Few-layer WSe_2 and monolayer WS_2 were exfoliated on the PDMS stamps then transferred on a sacrificed SiO_2/Si substrate. hBN flakes were exfoliated on 285-nm SiO_2/Si substrates by blue tapes. After annealing the substrate, a monolayer WS_2, sandwiched by hBN, was precisely aligned and transferred on top of the metasurface using a dry transfer technology (poly(bisphenol A carbonate) (PC) method) (Fig. S5c 1). The sample was then annealed at 250°C in an argon atmosphere for 2 hours to remove any residual PC, preparing the surface for subsequent transfers. Two pieces of few-layer WSe_2 of similar thickness were selected and subsequently laminated onto each terminal of the waveguide using a dry transfer technique (Fig. S5c 2). Following this, MoO_3 (5 nm)/Au (10 nm) charge transfer contacts were fabricated on the few-layer WSe_2 flakes through the standard photolithography and lift-off processes, ensuring effective ohmic contact for photocurrent detection (*1*) (Fig. S5c 3). Then two hBN flakes (~ 15 nm) were picked up and transferred onto the WSe_2 photodetectors to protect the channel during the following fabrication process and VMP device measurements (Fig. S5c 4).

Far-field characterisation of scattered light from chirality-selective meta-waveguide

A focused laser beam was employed to demonstrate the optical coupling and directional routing capabilities of the fabricated meta-waveguide (Fig S6). The bright spots at the centre of the image represent the primary beam spots. For σ^- incidence, light is coupled and routed to the left side of the meta-waveguide, whereas for σ^+ incidence, light is directed to the opposite side.

Directional coupling intensity variation as illuminating position.

Under ideal conditions with homogeneous illumination, both ports exhibit identical coupling and light routing, as demonstrated in Fig. 2b. However, we observe that a focused beam with limited coverage of the metasurface region can lead to intensity variations, as seen in the laser demonstration above (Fig. S6), where the far-field outcoupled intensity differs between the two polarisations. This discrepancy may arise from the precise location of the focused beam spot. To investigate this effect, we simulate small area illumination situation. For the pump wavelength of 1240 nm, it corresponds to a theoretical Airy disk beam diameter of ~2 μm. For our metasurface with pitch of 240 nm, such beam spot covers roughly about 8x8 nanopillars, covering at least three full phase variation cycles from 0 to 2π (Fig. S2a), which is sufficient for the metasurface gratings to couple light into waveguides, as can be seen in simulation results in Figs. 2d, S3 and S7b. As illustrated in Fig. S7a, the beam spot may be centered on the metasurface region or slightly offset to one side. The simulation results (Fig. S7b) show the normalised directional coupling intensity as a function of the beam's central position. When the beam spot is shifted to the left (right) side, σ^- (σ^+) excitation results in stronger coupling to the left (right) port. This behavior can be attributed to pillar perturbation and outcoupling effects. Within the illuminated region, the metasurface pillars perform similarly for both polarisations, differing only in their provision of opposite linear momenta to couple light into the waveguide. However, "unused" pillars along the propagation path perturb or outcouple some of the guided light, reducing the total intensity. Consequently, off-center illumination leads to measurable intensity differences between the two ports.

Optical setup configuration for PL and SHG characterisations

Figure S8 illustrates the optical setup used for both meta-waveguide characterisation and WS_2 PL (Figs. S9b,9c,9d) and SHG measurements (Figs. S9e,9f,9g, S10). For meta-waveguide characterisation, a 620-nm laser is employed for illumination. The light scattered by the grating coupler is captured by a camera after passing through a polarisation filter. In PL measurements, a supercontinuum laser source is utilised for near-resonance excitation, while a femtosecond laser is used for SHG measurements. Both laser signals are pre-cleaned using appropriate filters: a tunable filter for the supercontinuum excitation in the visible range and a 1000-nm long-pass filter for the NIR wavelength. Before reaching the detectors (camera or spectrometer), a second set of filters is applied to further refine the laser signals: a 600-nm long-pass filter for PL measurements and a 700-nm short-pass filter for SHG.

SHG wavelength sweep and two-photon luminescence

Figure S10 presents the results of excitation wavelength (photon energy)-dependent SHG measurements. At a fixed excitation power of approximately 10 mW, the SHG signal reaches its maximum near the excitonic bandgap. Any deviation in the photon energy of the excitation, whether an increase or decrease, leads to a significant drop in SHG intensity, particularly at higher photon energies (shorter wavelengths). More specifically, the SHG signal is further suppressed for wavelengths shorter than 610 nm, which can be attributed to the enhanced two-photon absorption efficiency in monolayer WS_2 around 593 nm, as reported in previous studies (*2*). Since the SHG photon energy lies above the bandgap, it may also be reabsorbed by the WS_2 monolayer. Overall, the two-photon luminescence peak appears at approximately 618 nm.

Photodetector response to electrical bias and incidence intensity

As shown in Fig. S13, we first performed electrical characterisation of the few-layer WSe_2 device under varying laser powers, ranging from 10 nW to 1 μW. The resulting I-V curves indicate that the device operates as a phototransistor, with the photocurrent increasing as the laser power rises, thereby demonstrating the functionality of 620 nm detection. We further demonstrated the on-chip near-field detection according to the setup in Fig. S14a. In Fig. S14b, the rise and fall of photocurrent (blue lines) is corresponding to the polarised laser on/off states. The decreasing trend in photocurrent with reduced laser power aligns with the I-V results in Fig. S13. We note the photocurrent drop at the same laser power (from 700 pA at 1uW in I-V measurement to 48 pA in the ON-OFF results) is likely attributed to meta-waveguide coupling and routing loss. Notably, even at low excitation power of 10 nW, the photocurrent exhibits sensitivity to the polarisation state of the input laser.

Laser ‘On’ and “Off” and photodetector “On” state definitions

Because of the finite beam diameter (~5 mm), the transitions between laser “On” and “Off” states are not perfectly instantaneous. As shown schematically in Fig. S15, the mechanical chopper introduces intermediate partial-transmission states. To characterise the actual laser on/off timing, we directly measured the transmitted beam in real time using an avalanche photodiode (SPCM-AQRH-14-FC, Excelitas). This leads to the sine-wave-like photocurrent responses observed in Fig. 4c and 4d. To capture the average photodetector performance, we defined the “On” state statistically: the median value and ± one standard deviation within the top 20% of the response range (Fig. S16). Using the same approach, we also extracted the error bars shown in Fig. 4e.

Supplementary Note 1. Nonlinear valley selection rule in monolayer TMDCs

Two-photon interband transitions in monolayer TMDCs are governed by symmetry constraints that extend the valley-selective behaviour observed in one-photon processes. The transition amplitude involves a product of dipole matrix elements:

$$\langle \psi_c | \hat{\mathrm{P}}_{\pm} | \psi_j \rangle \times \langle \psi_j | \hat{\mathrm{P}}_{\pm} | \psi_v \rangle$$

Where ψ_c and ψ_v are conduction and valence band states, ψ_j is an intermediate virtual state, $\hat{P}_{\pm} = \hat{P}_x + i\hat{P}_y$ corresponds to σ^+ or σ^- circularly polarised light.

To determine whether this two-photon transition is allowed, we apply the threefold rotational symmetry operator $\hat{c}_3$ (a 120° rotation about the z-axis). This symmetry is intrinsic to the crystal structure of monolayer WS_2, which belongs to the D_{3h} point group. The presence of C_3 symmetry constrains how both the electronic states and optical operators transform under rotation (*3*).

Under C_3: Bloch states transform as $\hat{C}_3 | \psi_\alpha \rangle = exp(-i2\pi s_\alpha/3) \times | \psi_\alpha \rangle$, where s_α is the effective angular momentum quantum number of states α (c, v, or j). The momentum operator transforms as

$$\hat{C}_3 \hat{P}_{\pm} \hat{C}_3^{-1} = exp(\mp i2\pi/3) \times \hat{P}_{\pm}$$

Inserting identity operators $\hat{C}_3 \hat{C}_3^{-1}$around each matrix element and applying these transformations yields:

$$\langle \psi_c | \hat{\mathrm{P}}_{\pm} | \psi_j \rangle \rightarrow \exp\left(-\frac{i2\pi(s_c - s_j \pm 1)}{3}\right) \times \langle \psi_c | \hat{\mathrm{P}}_{\pm} | \psi_j \rangle$$

$$\langle \psi_j | \widehat{\mathrm{P}}_{\pm} | \psi_v \rangle \rightarrow \exp\left(-\frac{i2\pi(s_j - s_v \pm 1)}{3}\right) \times \langle \psi_j | \widehat{\mathrm{P}}_{\pm} | \psi_v \rangle$$

Multiplying these phases gives the total symmetry constraint:

$$\exp\left(-\frac{i2\pi(s_c - s_v \pm 2)}{3}\right)$$

For the transition to be symmetry-allowed, this phase must equal. This condition directly determines whether a given two-photon process is allowed at a specific valley.

At the K valley: $s_c = 0$ (conduction band), $s_v = +2$ (valence band).

For two σ^+ photons: $\exp\left(-i2\pi(0-2+2)/3\right) = \exp(0) = 1$ →transition allowed

At the K' valley: $s_c = 0$, $s_v = -2$.

For two σ^- photons: $\exp\left(-i2\pi(0-(-2)-2)/3\right) = \exp(0) = 1$ →transition allowed

Thus, the valley selection rule for two-photon transitions mirrors that of one-photon processes: transitions are allowed only when the photon helicity matches the valley-specific angular momentum difference. This symmetry constraint also governs resonant SHG, ensuring that SHG inherits both the valley selectivity and excitonic character of the corresponding one-photon transitions. The SHG intensity peaked when the excitation wavelength approached twice the excitonic transition wavelength of WS_2 (Fig. 3b), consistent with resonant enhancement.

Recent experimental demonstrations of the nonlinear valley selection rule have shown how valley imbalance arises directly in the nonlinear process (*4*). Under optical pump, the electronic structure is modified through the optical Stark effect (*5*) and the Bloch–Siegert effect(*6*), which act asymmetrically on the two valleys. Specifically, σ^- excitation drives the K valley via the optical

Stark effect, and simultaneously the K′ valley via the Bloch–Siegert effect, thereby breaking time-reversal symmetry. This valley-contrasting perturbation results in an imbalance between the two valleys and gives rise to a helicity-dependent nonlinear optical susceptibility, underpinning the observed valley-dependent SHG.

Supplementary Note 2: Design principle of geometric phase metawaveguide

On top of the metawaveguide chip, the metasurface diffractive grating provides a lateral linear momentum k_G, enabling free-space light coupling into a waveguide mode by matching the incident wave vector k_{in} with the propagation constant of the fundamental waveguide mode (Fig. S2a). In our simulation, illumination was modelled using an array of coplanar electric dipoles positioned above the meta-atoms, emulating PL and SHG processes. (Fig. 2a). This effectively approximates normal-incidence excitation (transverse component of k_{in} is 0) to the meta-waveguide. The momentum conservation law gives $k_G = n_{eff} \times k_0$, where n_{eff} is the effective index of the waveguide mode (1.7834 in this work), and k_0 is the free-space wavenumber.

To achieve circular polarisation-selective coupling, nanoantennas were designed as subwavelength half-wave plates, imparting a Pancharatnam–Berry phase of $\pm 2\theta$, where θ is the antenna rotation angle and the sign ± depends on the incident circular polarisation states (*7*). In a geometric phase grating, the constant phase gradient is defined by the transverse momentum, expressed as $k_G = \pm 2\theta/p$, where p is the grating pitch. In our practical design, accounting for nanofabrication resolution, we selected a pitch of p = 240 nm, which corresponds to a rotation angle $\theta = 124.3^{o}$, yielding at least three discrete geometric phase levels (within 0-2π phase cycle) for the circular-polarisation-selective unidirectional coupling grating.

We further performed a parametric sweep using rigorous coupled-wave analysis (RCWA) to identify optimal nanoantenna dimensions. Amorphous silicon (a-Si) was selected as the nanoantenna material, positioned atop a silicon nitride (Si_3N_4) waveguide with a thickness of 350 nm (Fig. S2b). Based on the previously determined grating pitch of 240 nm, we varied the nanopillar length and width, and evaluated the resulting phase retardation (Fig. S2c) and cross-polarisation efficiency (Fig. S2d) for transmitted light. The optimised structure—comprising a nanoantenna pillar with height of 250 nm, length of 143 nm, and width of 98 nm—was selected based on performance metrics and fabrication feasibility. Notably, the design is compatible with high-resolution electron beam lithography.

Supplementary Note 3: Metawaveguide modelling under different illumination conditions

For the metawaveguide modelling, we examine its performance under two different illumination conditions: coplanar dipolar array and plane wave. The coplanar dipolar array reflects more closely the on-chip excitation of PL and SHG emission profiles (Figs. 3 and 4), while plane wave illumination is closer to our laser beam characterisation of the metawaveguide (Figs. 2f and 2g, Fig. S6).

1) Coplanar dipole array illumination

In practice, the TMDC material is pumped with a focused laser beam. To model this, we use a coplanar array of dipoles to represent the SHG emission (Fig. S3a). The incident beam is assumed to have a Gaussian intensity profile with a diameter D. For a pump wavelength of 1240 nm, this corresponds to an ideal beam diameter $D \sim 1.7$ μm. Because we employ a relatively low-NA objective lens (NA = 0.45), the in-plane phase of incident field can be approximated as uniform. As our main interest lies in circularly polarised excitation, the overall SHG intensity distribution is uniform with respect to crystal orientation. In a nonlinear process, however, the induced emission profile approximately follows the Gaussian envelope of the pump, but with the squared amplitude of the electric field (Fig. S3b). To capture this effect, we model the SHG source as an array of dipoles with ~40 nm spacing distributed across the illuminated region (2 μm). Each dipole is assigned a Gaussian-weighted amplitude while maintaining a fixed relative phase (Figs. S3c and S3d), thereby representing the coherent SHG emission from the flake.

The radiation profile at the metasurface interface, separated from the dipole plane by a spacer of thickness d, is obtained as the superposition of the vector fields from all dipoles. The dipoles are confined to the x–y plane and radiate along the z-axis. Left-handed circular polarisation (σ^-) as example, the dipole field is defined as $E_{LCP} = \begin{bmatrix} 1 \\ -i \\ 0 \end{bmatrix}$. We examined the co-polarisation component and found that, within the tested propagation distance of up to one micrometre, the resulting emission pattern remains essentially disk-shaped (Fig. S3e). This behaviour arises because dipoles near the beam centre contribute significantly to the electric field profile in the metasurface surface plane than those at edges, while the overall symmetry strongly suppresses interference effects on the length scale. Building on this model, we implemented the same dipole distribution in COMSOL to verify the performance of our chirality-selective meta-waveguides. For computational efficiency, we restricted the simulation to 11 rotating nanopillars in each row and 10 rows in total, ensuring the array was still larger than the illuminated dipole region (Fig. S3f). The simulated results confirm highly directional routing of the chiral photons for dipolar arrays positioned at distances ranging from 10 nm (polarisation selectivity ~80%) to 1 μm (>85%) above the metawaveguide surface (Figs. S3g and S3h).

2) Plane wave illumination

Full 3D modelling becomes increasingly computationally demanding as the number of nanoantennas grows. For the experimental case of laser characterisation of the metawaveguide with a low-NA objective (Figs. 2f, 2g, and S6), the illumination can be well approximated by a plane wave. Under this condition, the simulation can be significantly simplified by applying periodic boundary conditions along the x-axis and modelling only a single row of antennas in a slab-waveguide configuration (Fig. S4a). The corresponding simulation results, shown in Fig. S4b (top and side views), demonstrate ultra-high (>98%) polarisation selectivity. When a σ^- plane wave is used as the pump (with a port–metasurface distance of 1 μm), the Ex field, aligned with the fundamental TE mode of the waveguide, exhibits strong coupling and highly directional routing to the left.

Importantly, these results are consistent with those in Fig. 2b, where a linear dipole array (spacing = 240 nm, d = 10 nm) was used together with periodic boundary conditions along the x-axis. We note that when the emission sources are positioned very close to the surface (d <10 nm), the dipole array behaves similarly to a plane wave due to minimal near-field interference. However, increasing the separation (d > 100 nm) introduces the interference effect, causing the effective excitation to deviate from the idealised plane-wave illumination.

Supplementary Note 4: Near-field absorption of few-layer WSe_2 integrated with a Si_3N_4 waveguide with and without a grating coupler

To evaluate the near-field absorption of WSe_2 integrated with our Si_3N_4 waveguide platform, we performed numerical simulations under two configurations: without and with grating couplers (Figs. S12 a, b). For a bare Si_3N_4 waveguide (Fig. S12a, upper panel), the transmittance remains >0.99 with negligible propagation loss. When a 10-μm-long few-layer WSe_2 flake is placed on top (Fig. S12a, lower panel), the guided mode experiences strong absorption, reducing the transmittance to 0.511, leading to WSe_2 absorption of ~0.483. When a grating coupler is introduced (Fig. S12b, upper panel), the waveguide transmittance decreases to 0.484, primarily due to outcoupling losses (~0.516). Adding the same 10-µm-long WSe_2 on top of the grating region (Fig. S12b, lower panel) further reduces the transmittance to 0.319. In this case, the overall propagation loss increases to 0.655, with ~0.358 directly attributable to WSe_2 absorption.

These results confirm that WSe_2 exhibits strong near-field absorption in both bare waveguide and grating-assisted configurations. Importantly, the presence of the grating coupler does not suppress absorption but rather provides an additional pathway for waveguide coupling and loss. This demonstrates the high absorption efficiency of WSe_2 photodetectors, reinforcing their robust utility in compact on-chip light detection.

Supplementary Note 5: Simulated polarisation dependence in Fig. 4e.

The observed non-ideal sine waveform in Fig. 4c primarily arises from phase retardation mismatch in the nanopillar metasurface, deviating from the ideal half-wave plate condition due to dielectric environment change caused by the transferred heterostructure (hBN-WS_2-hBN). To verify this effect, we performed a simulation configured for circularly polarised light detection (Fig. S17a). A linearly polarised beam passes through a quarter-wave plate (QWP) to generate circular polarisation, which then propagates through the target phase retarder (the nanopillar metasurface). For ideal π phase retardation, the output detected through either an LCP or RCP analyser yields a sinusoidal response, as shown by the shaded curve. In contrast, when the phase retardation is set to 0.85π, the simulated detection curve deviates from the ideal sine-wave profile and closely matches the experimental observation (Fig. S17b).

We therefore attribute the photocurrent clamping observed in Fig. 4e to slight deviations in the nanopillar phase response from the optimised design, induced by dielectric environment changes introduced by the transferred heterostructure (hBN–WS_2–hBN). Despite this minor deviation, we experimentally observed pronounced valley polarisation contrast, enabling high-fidelity on-chip processing of valley-multiplexed images (Figs. 4g–4i).

Supplementary Note 6: Valley information processing experimental setup

The experimental setup used for characterisation is illustrated in Fig. S18. A linearly polarised laser beam is first split into two channels via a beam splitter. Each channel is then converted into left- and right-circularly polarised (LCP and RCP) states using dedicated quarter-wave plates. Two data acquisition (DAQ)-controlled shutters, driven by digital input/output (DIO) signals, regulate the sequential ON–OFF timing of each channel. The two beams are incoherently recombined and directed onto the valley optoelectronic nanocircuit for on-chip valley information processing.

Valley-dependent chiral photons in-situ generated by the pump beams are waveguide coupled and detected by on-chip photodetectors. The resulting photocurrents are amplified using a low-noise current preamplifier (SR570) and converted into analogue voltage signals. These voltages are recorded by the DAQ system, and the time-sequence data are processed into images on a computer.

As a proof of concept, we implemented pixel-by-pixel signal reconstruction using Python scripts that synchronized shutter control with photodetector readouts. An example is shown in the top-right inset: red bars indicate a line scan with ON/OFF DIO triggers (S1, S2; 25 ms per action), while blue bars represent the corresponding voltage signals. To mitigate artefacts from the photodetectors' slow response (Figs. 4c and 4d), a voltage threshold filter was applied in post digital data processing. Specifically, only voltages above 2.4 V (~80% of the peak value) were recorded as binary digit "1"; all others were assigned to "0". Upon completing a full scan, the input image patterns ("Koala" and "Kangaroo") were successfully reconstructed, as shown at the bottom of Fig. S18.

Figs

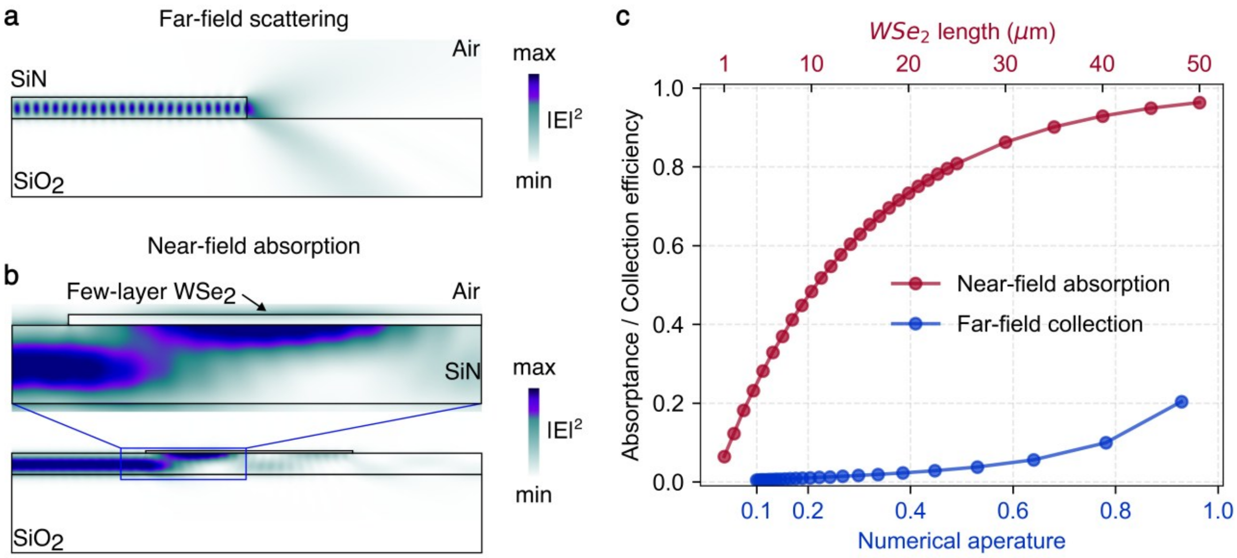

Fig. S1. Collection of waveguide-routed light in the far-field/near-field regime. Electric-field energy distribution for (**a**) scattered light at the waveguide end and (**b**) light in the presence of a thin WSe_2 layer. (**c**) collection efficiency as a function of numerical aperture for far field and WSe_2 length for near field respectively. Simulation parameters: Si_3N_4 waveguide on SiO_2 substrate, wavelength of 620 nm, Si_3N_4 thickness of 350 nm, and WSe_2 thickness of 3 nm (approximately 5 layers). Red and blue dots represent simulation data for the two conditions, respectively.

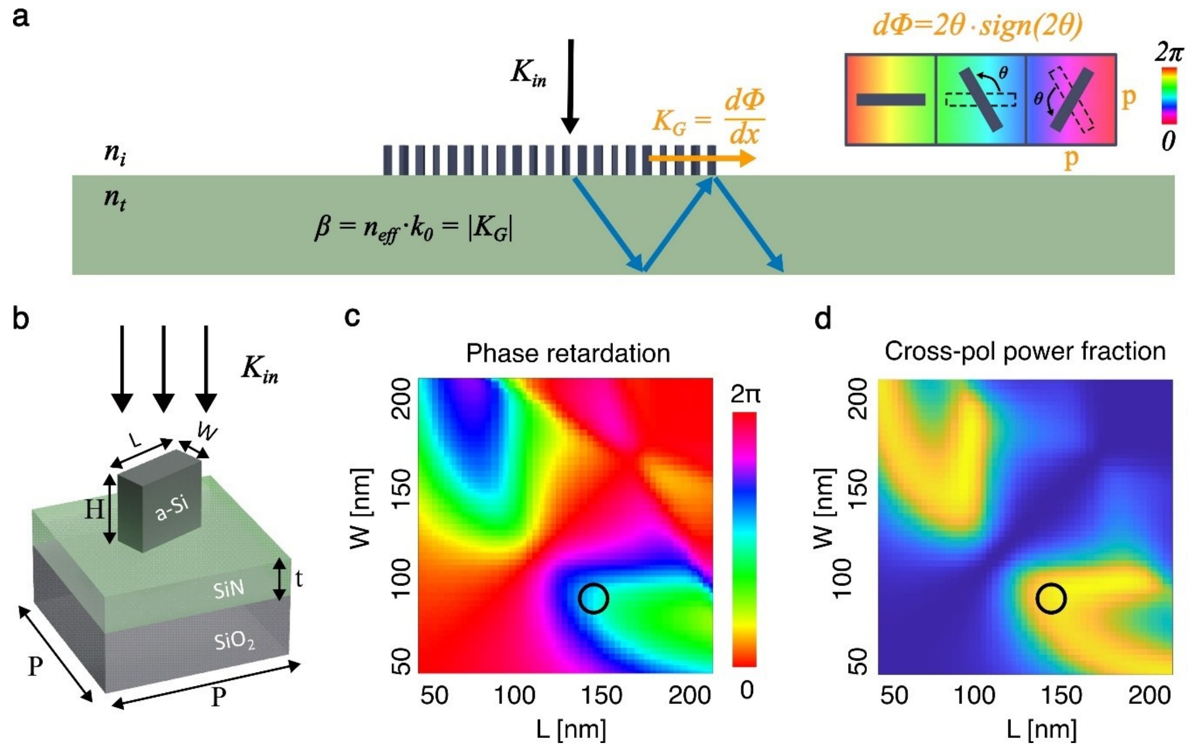

Fig. S2. Operating principle and nanostructure design of the metasurface diffractive grating. (**a**) Schematic illustration of a geometric phase metasurface-based unidirectional light coupling to a waveguide. Inset, top view of rotated nanopillars for phase impartment. (**b**) Meta-atom dimensions used for simulation. (c and d) Phase retardation (**c**) and polarisation conversion efficiency (d) of cross circular polarisation states. Circles in (c) and (**d**) highlighted the selected meta-atom dimensions.

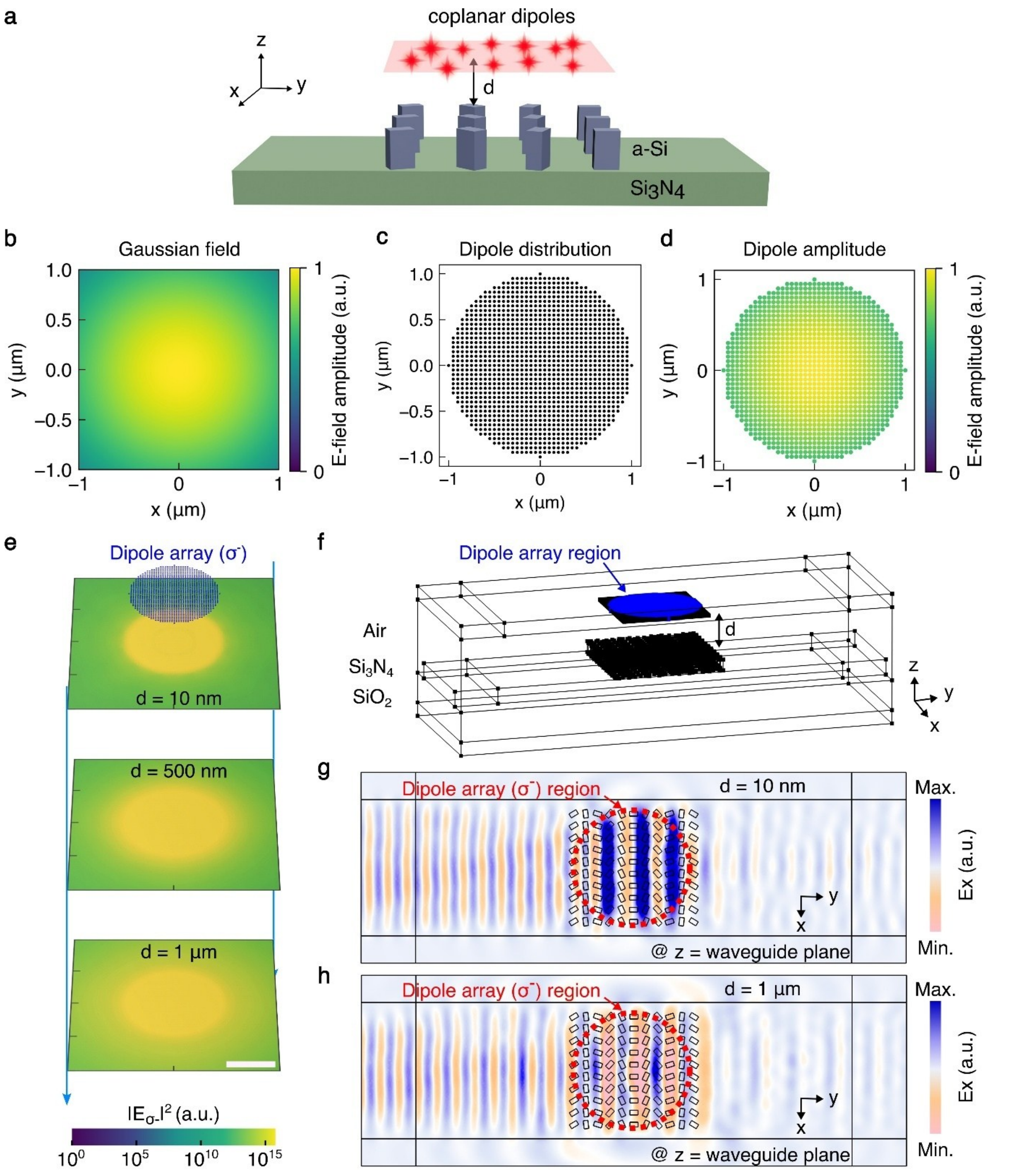

Fig. S3. Coplanar dipole array illumination. (**a**) 3D configuration of the proposed meta-waveguide structure, consisting of an a-Si metasurface on a Si_3N_4 waveguide supported by a quartz substrate (not shown). Coplanar electric dipoles are placed above the meta-atoms to represent illumination. (**b**) A squared Gaussian field profile representing the nonlinear emission field. (**c**) Spatial distribution of dipoles. (**d**) Coherent dipole array (in-phase) with varying amplitudes to emulate the SHG emission response. (**e**) Calculated σ^- radiation patterns at propagation distances of d = 10 nm, 500 nm, and 1 μm. (**f**) Numerical simulation with excitation dipole array distributed within a circular area of diameter of 2 µm. (g, h) Selective routing of σ^- photons to the left side of the waveguide at d = 10 nm and 1 µm, respectively.

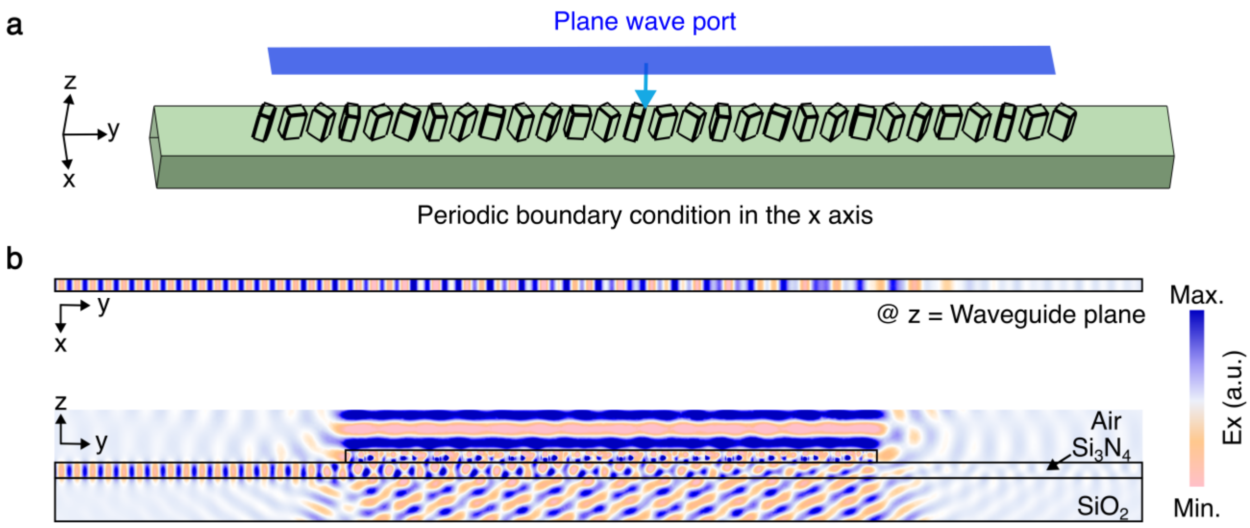

Fig. S4. Plane wave illumination. (**a**) Simulation model of a single row of nanopillars on a Si_3N_4 waveguide with periodic boundary conditions and σ^- plane-wave incidence. (**b**) Selective routing of σ^- photons to the left of the waveguide. The top (bottom) panel shows the top (side) view of the Ex- field distribution.

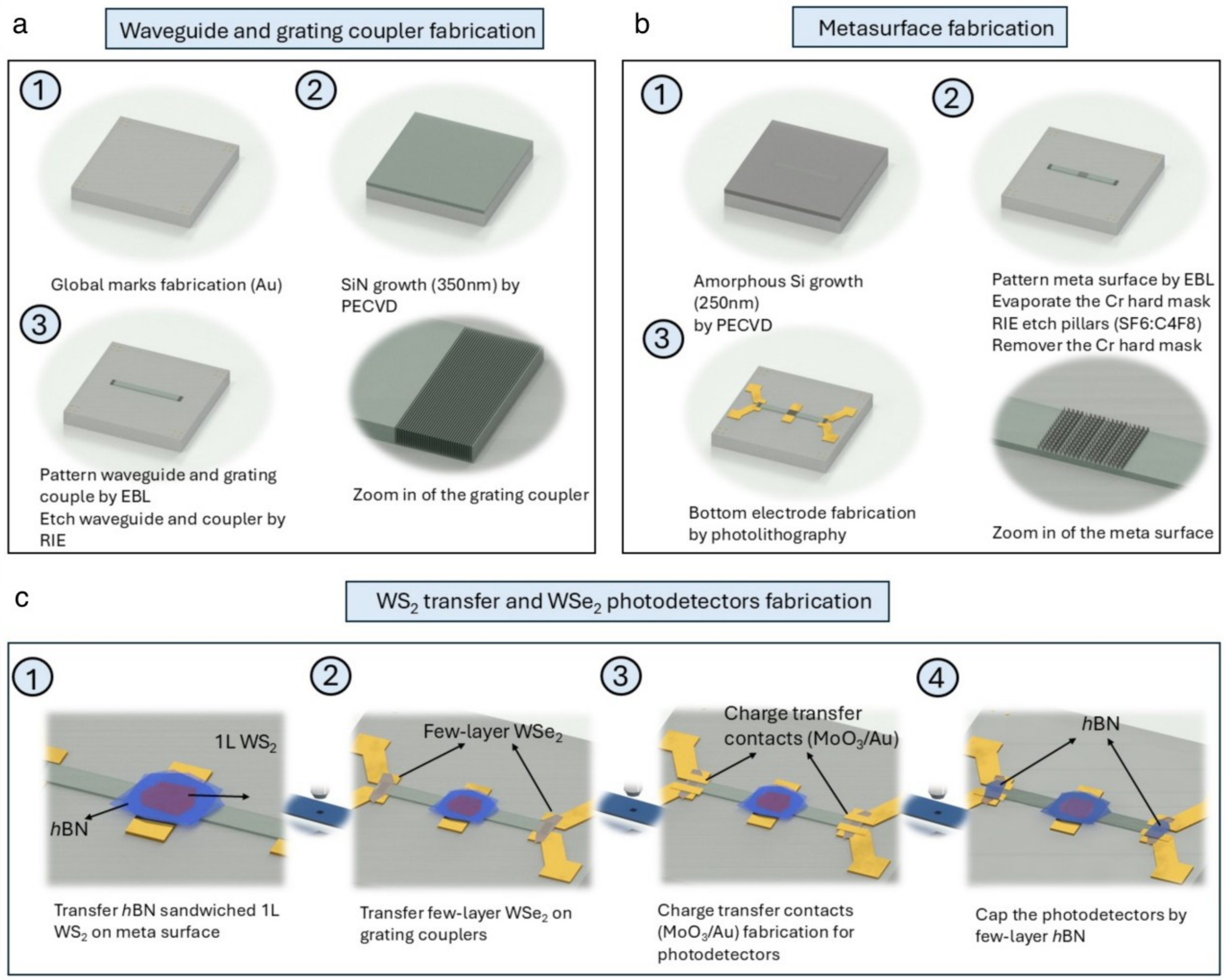

Fig. S5. Nanofabrication processes of the entire VMP device. (**a**). Waveguide and grating coupler fabrication. (**b**). Metasurface fabrication. (**c**). Photodetector fabrication.

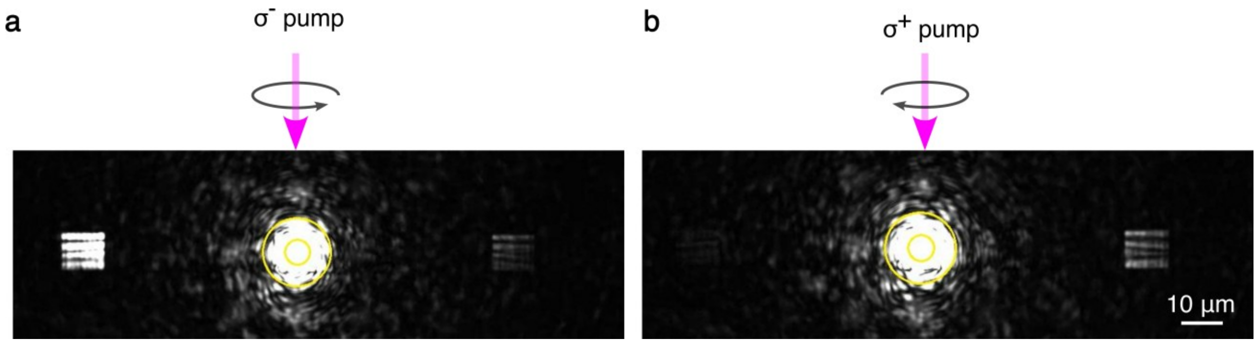

Fig. S6. Directional routing of circularly polarised laser at 620 nm. (**a**), (**b**) are monochromatic photographs of the scattered laser from metasurface and out-coupler regions. Yellow circles indicate the incidence location.

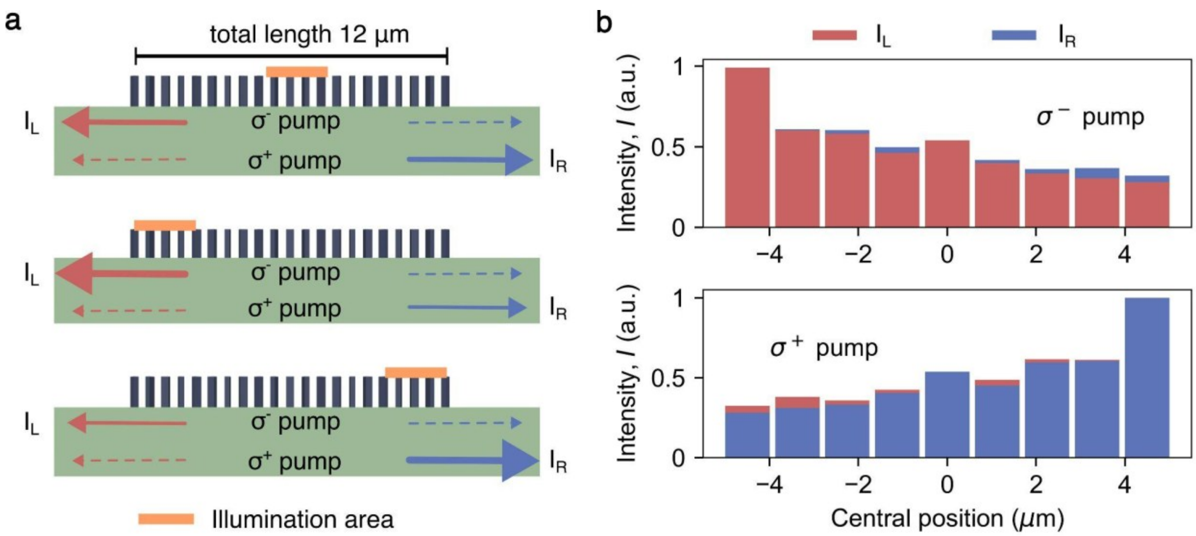

Fig. S7. Directional coupling intensity as a function of illuminating position. (**a**) schematics for beam spot on the centre, left and right side of the metasurface respectively. (**b**) simulated results for the directional waveguide coupling as beam spot central position.

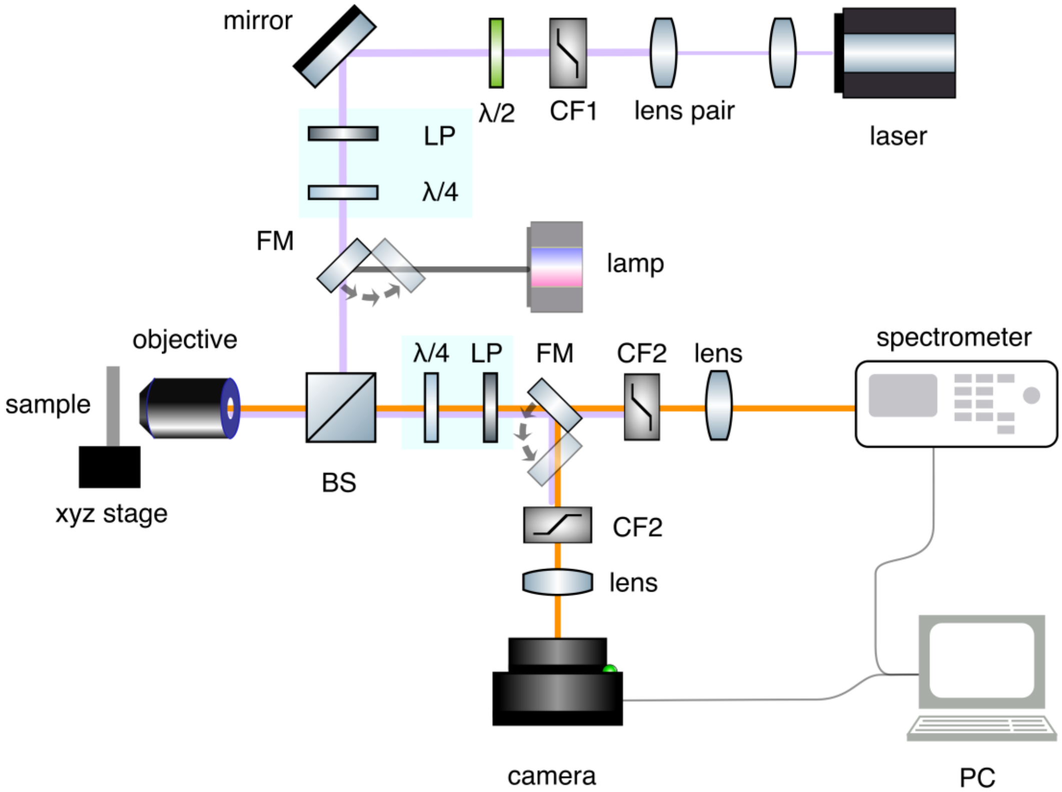

Fig. S8. Optical setup for meta-waveguide characterisation and PL/SHG spectral measurements. λ/2: half-wave plate; CF1: laser cleaning filter sets; LP: linear polariser; λ/4: quarter-wave plate; FM: flip mirror; BS: beam splitter; CF2: colour filter sets for detection. The two shade regions are circular polarisation generation and detection zones, in which λ/4 plates were on a stepper motor rotation mount for precise circularisation control.

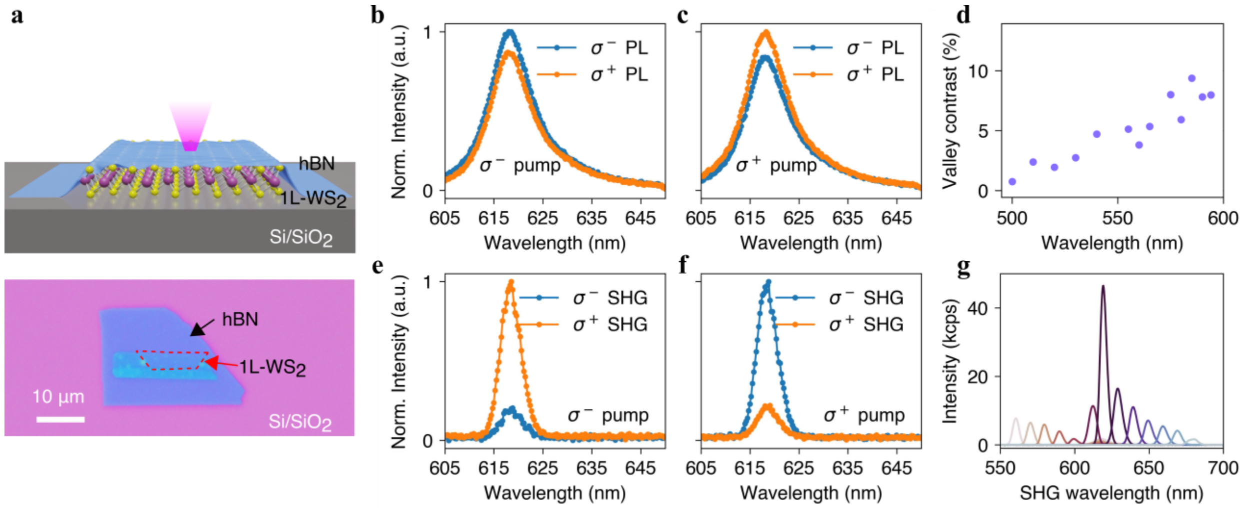

Fig. S9. Experimental characterisation of polarisation-resolved PL (upper) and SHG (lower) emissions from a monolayer TMDCs. (**a**) Schematic and optical image of a transferred monolayer TMDCs protected by a thin layer of hBN. (b-d) Polarisation-resolved PL spectra for (**b**) σ- and (**c**) σ+ polarisation pumps at the wavelength of 590 nm. Valley contrast is shown in (**d**) based on different excitation wavelengths. (**e-g**) SHG counterparts shown in full analogy to the PL characterisation in (**b–d**). The small co-polarisation components arise from the use of a beam splitter in a reflection optical setup, which introduces polarisation degradation in the measurement.

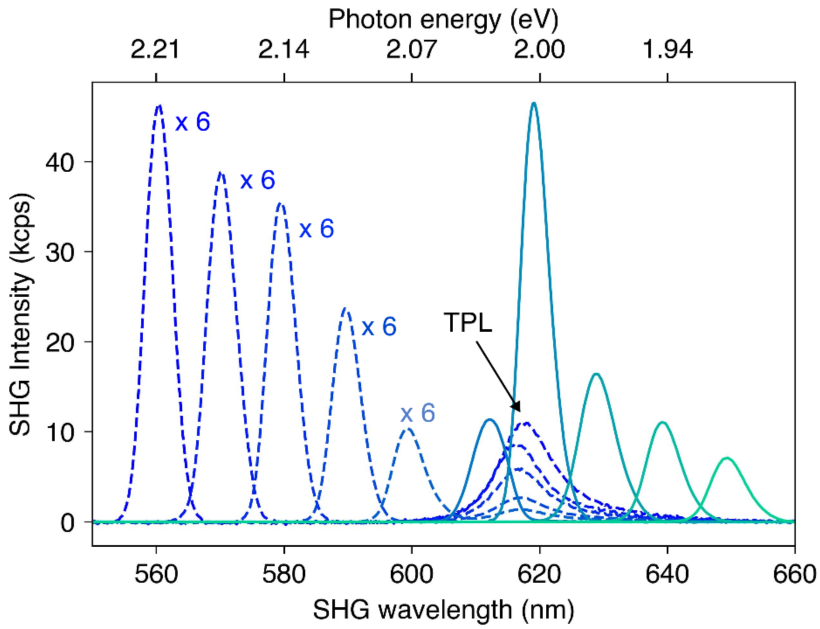

Fig. S10. Two-photon luminescence in SHG wavelength sweep measurement. The excitation wavelength starts at 1120 nm and increases in 20-nm steps, ending at 1300 nm. All wavelengths were measured at the same input power of ~10 mW. SHG signals for wavelengths below 1220 nm (dashed lines) are multiplied by a factor of 6 for clarity. Note that these data correspond to the same dataset presented in Fig. 3c.

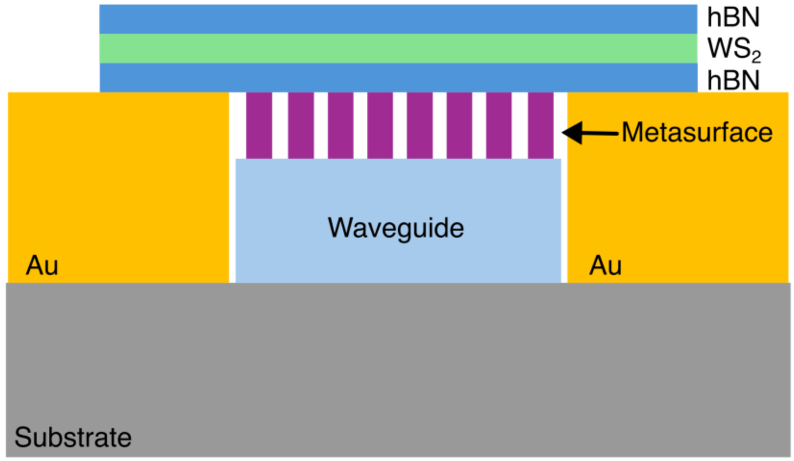

Fig. S11. Schematic for the cross section of the hBN/WS_2/hBN metasurface part.

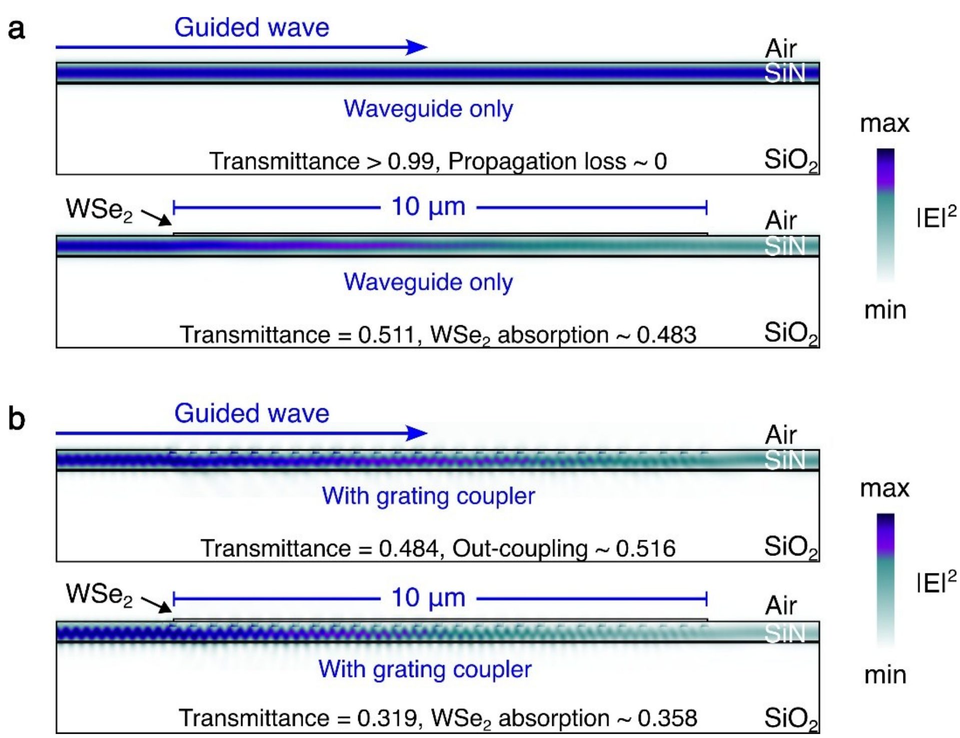

Fig. S12. Near-field absorption of few-layer WSe_2 integrated with a Si_3N_4 waveguide. (**a**) A bare Si_3N_4 waveguide with (lower) and without WSe_2 (upper). (**b**) Grating-assisted light absorption on a Si_3N_4 waveguide with (lower) and without the WSe_2 layer (upper).

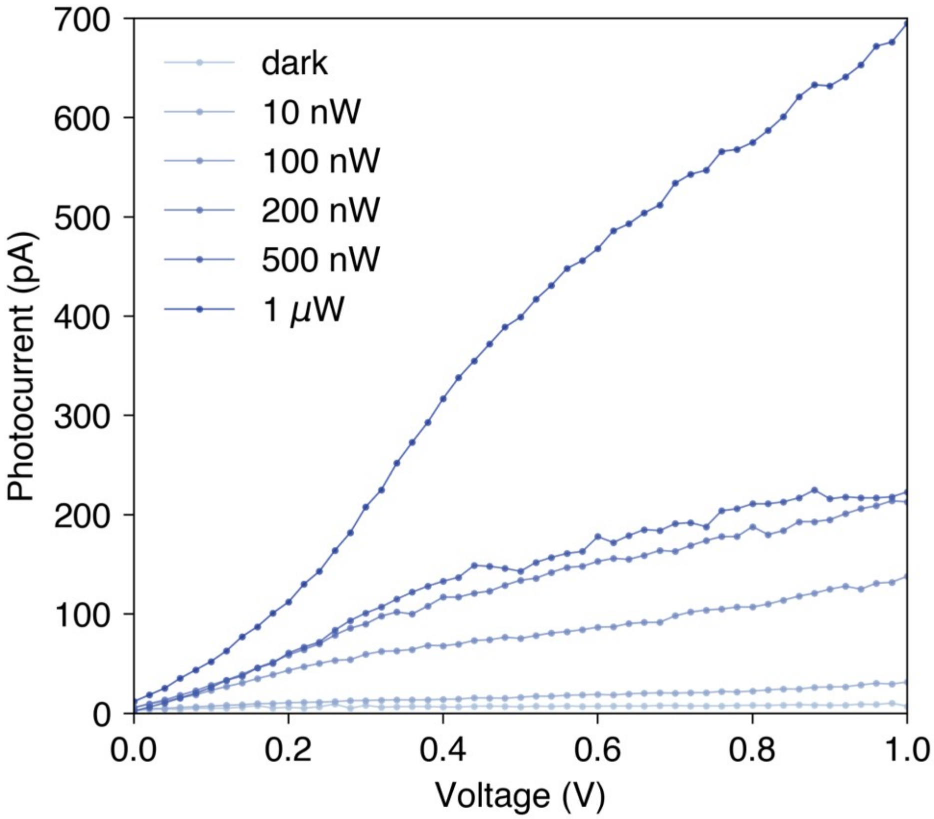

Fig. S13. Laser power dependent photocurrent measurements. I-V curves of the few-layer WSe_2 device in dark and under different illumination intensities (10 nW, 100 nW, 200 nW, 500 nW and 1 μW) without static electrical gating. 620-nm picosecond pulse laser illuminated directly on the photodetector.

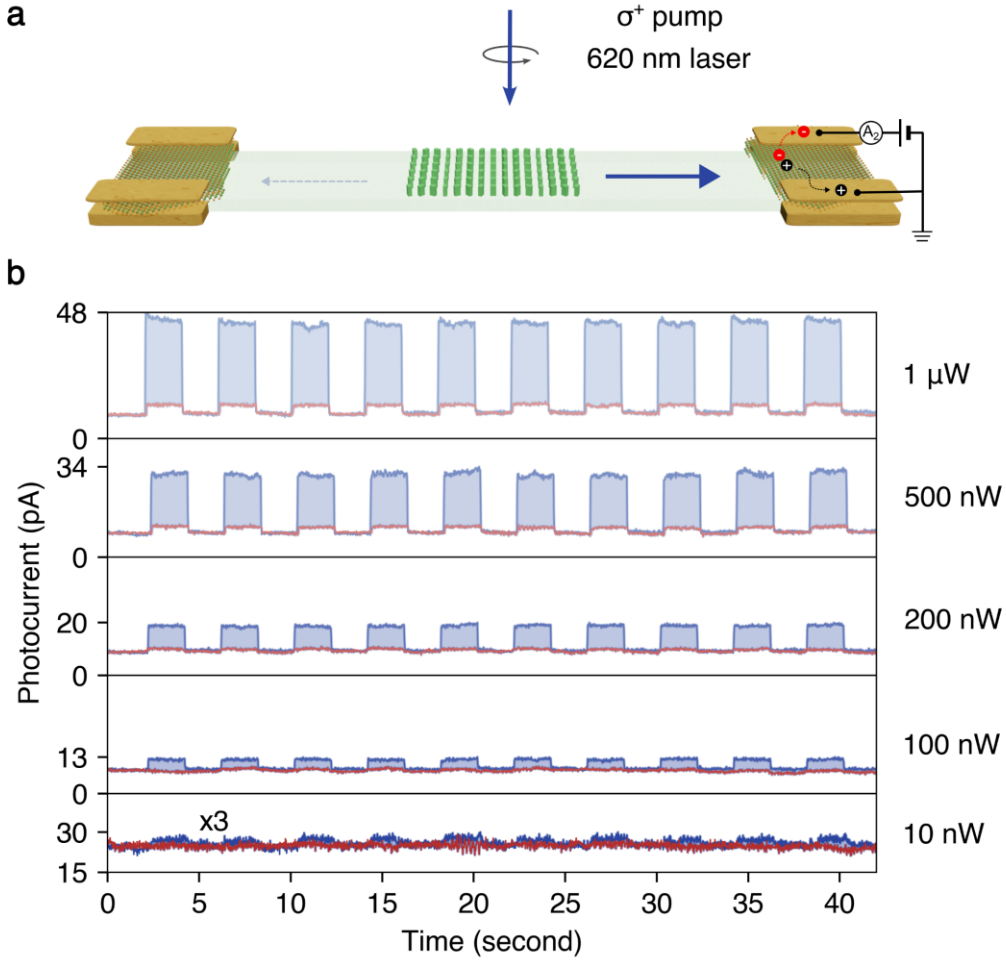

Fig. S14. Photodetector ON-OFF response at various laser excitation power. (**a**). Schematic of the photodetector response characterisation. The circularly polarised laser (620 nm) was focused on the meta surface and the photocurrent was measured at the end of the waveguide by a WSe_2-based photodetector. (**b**). Time-resolved photo response of the few-layer WSe_2 device with different laser power at V_{ds} of 1 V. The blue lines represent σ^+ polarisation of pump, whereas the red lines represent under σ- polarisation pump (not shown in schematics). The Keithley 2450 was employed to monitor the photocurrent and a shutter was utilized to control the state (on/off) of the laser.

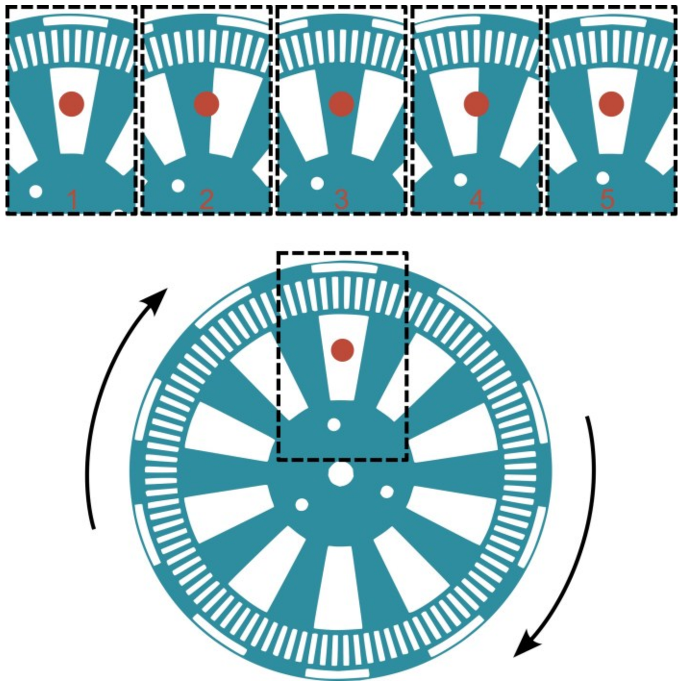

Fig. S15. Chopper and beam spot. Beam “On” (1 and 5), “Off” (3) and “Transition” (2 and 4) states are illustrated with respect to the chopper rotation.

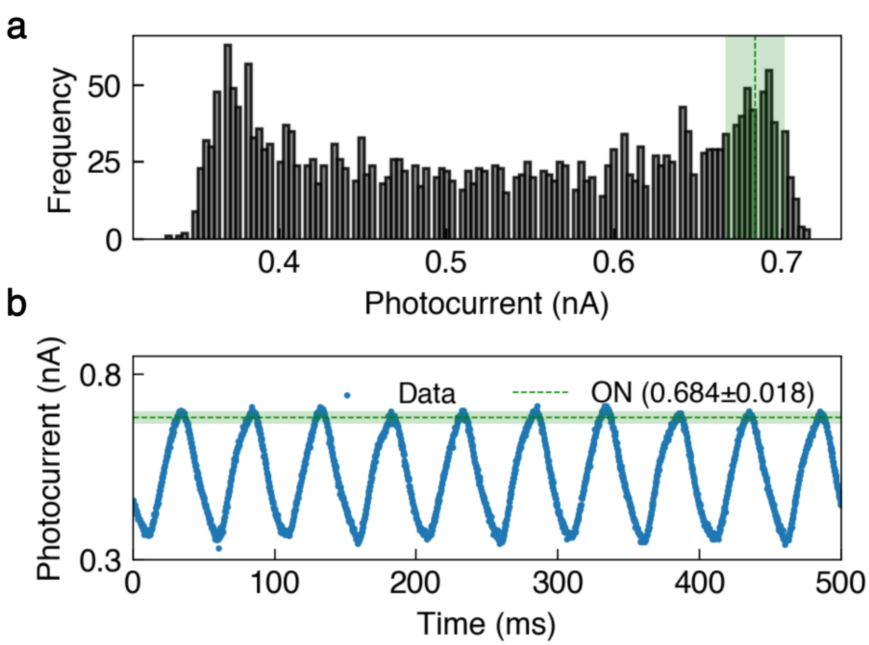

Fig. S16. Determination of the “On” state. (**a**) Frequency histogram of photocurrent values over 10 ON–OFF cycles. The median value and ± one deviation within the top 20% range are used to define the “On” state. The green dashed line and shaded area indicates this region. (**b**) Original oscilloscope data with the defined “ON” state highlighted.

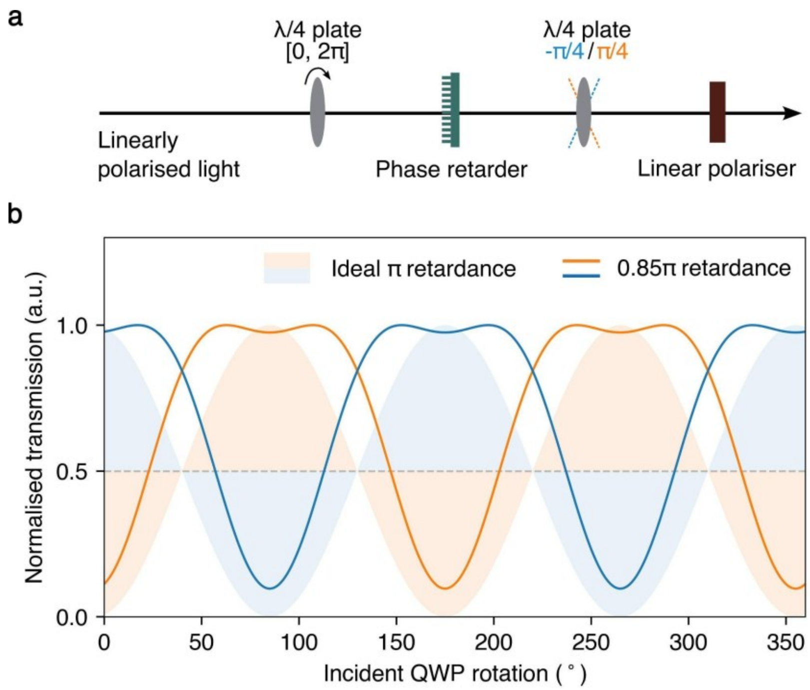

Fig. S17. Simulated polarisation dependence in Fig. 4e. (**a**) A schematic of the polarisation setup: incident light, prepared via wave plates, passes through a phase retarder and a circular polarisation analyser. (**b**) Normalised transmission of circular-polarisation-filtered light signals. Red and blue colours in the plot represent LCP and RCP respectively. The filled region shows the simulation results based on an ideal half-wave-plate phase retarder

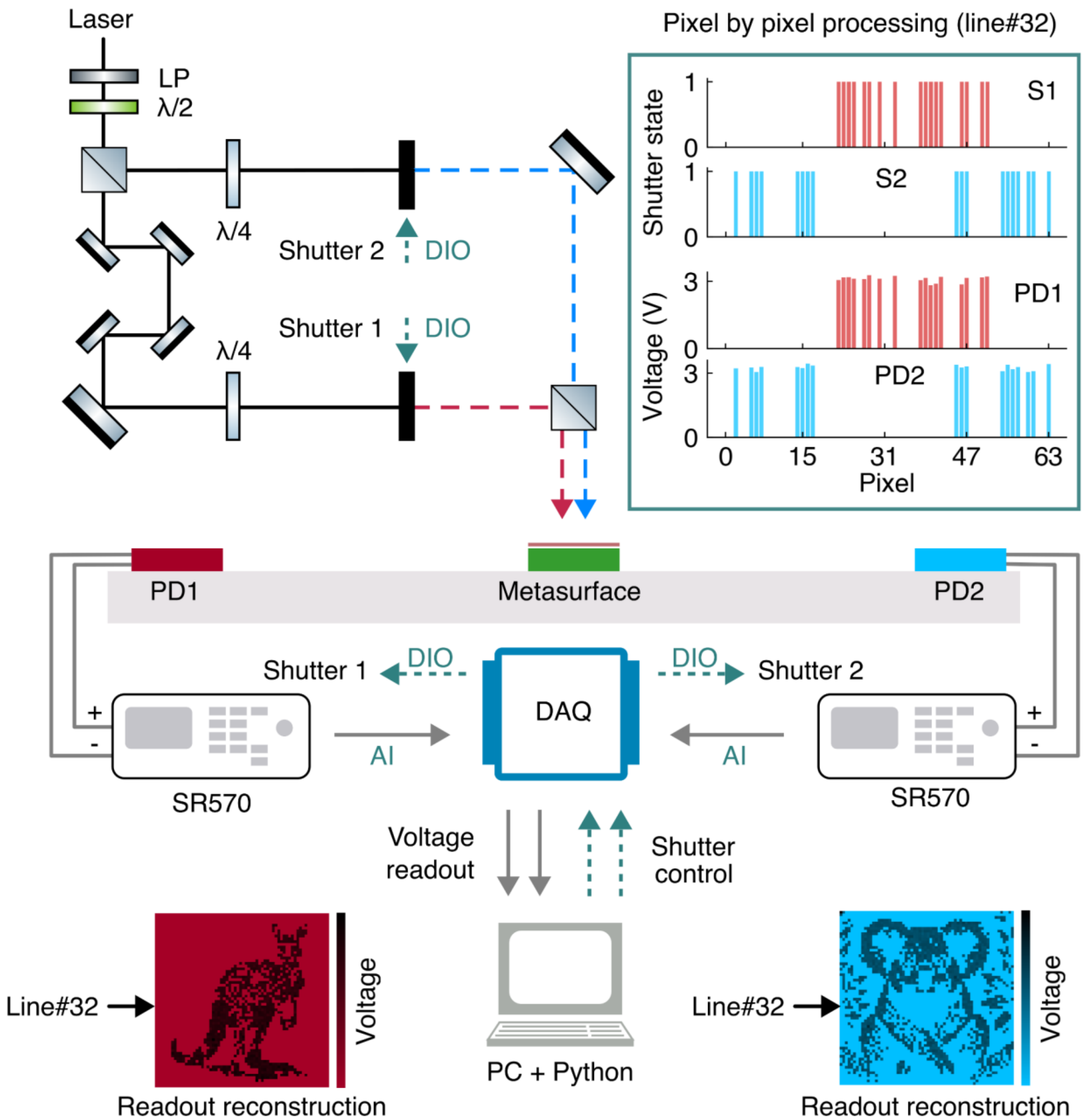

Fig. S18. Valley information processing experimental setup. Optical and electrical schematics for valley-state encoded information detection. The inset shows the experimental voltage outputs from the low-noise current preamplifier at line #32 for PD-1 and PD-2, respectively. AI, analogue input; DIO, digital input and output.

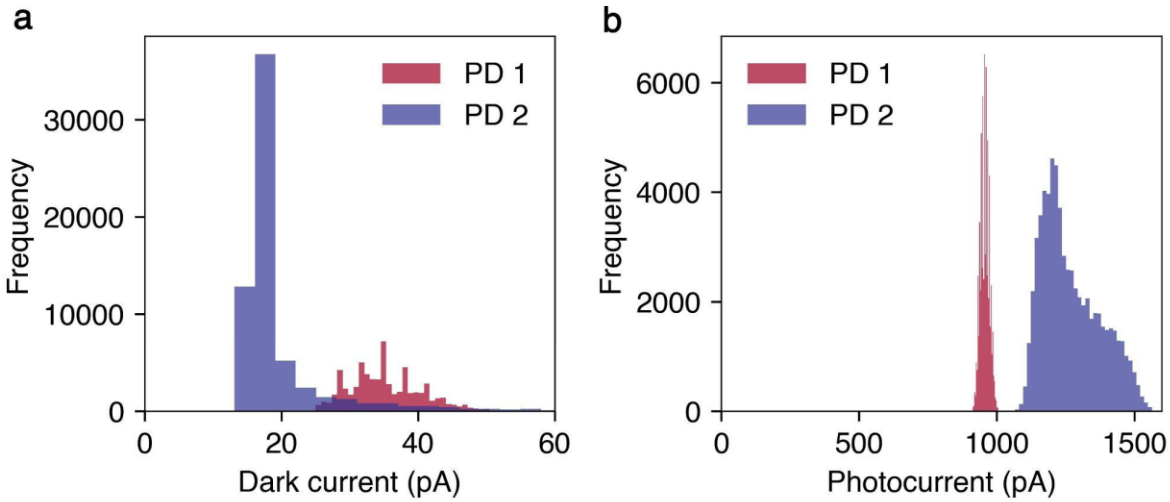

Fig. S19. Frequency histogram of dark current and target detection photocurrent for PD-1 and PD-2 in the mapping results in Figure 4.

References

1. Y.-H. Chen *et al.*, P-Type Ohmic Contact to Monolayer WSe_2 Field-Effect Transistors Using High-Electron Affinity Amorphous MoO_3. *ACS Applied Electronic Materials* **4**, 5379-5386 (2022).
2. J. Xiao *et al.*, Nonlinear optical selection rule based on valley-exciton locking in monolayer WS_2. *Light: Science & Applications* **4**, e366-e366 (2015).
3. K. L. Seyler *et al.*, Electrical control of second-harmonic generation in a WSe_2 monolayer transistor. *Nature Nanotechnology* **10**, 407-411 (2015).
4. P. Herrmann *et al.*, Nonlinear valley selection rules and all-optical probe of broken time-reversal symmetry in monolayer WSe_2. *Nature Photonics*, 1-7 (2025).
5. J. Kim *et al.*, Ultrafast generation of pseudo-magnetic field for valley excitons in WSe2 monolayers. *Science* **346**, 1205-1208 (2014).
6. E. J. Sie *et al.*, Large, valley-exclusive Bloch-Siegert shift in monolayer WS_2. *Science* **355**, 1066-1069 (2017).
7. X. Guo, Y. Ding, X. Chen, Y. Duan, X. Ni, Molding free-space light with guided wave–driven metasurfaces. *Science advances* **6**, eabb4142 (2020).